

Atomic imaging for hydrogen and boron aggregates in boron-doped diamond by spectro-photoelectron holography

Received: 5 August 2025

Accepted: 23 February 2026

Published online: 05 March 2026



Hiroto Tomita¹✉, Wataru Hosoda², Takumi Taniguchi², Hirokazu Fujiwara^{3,4}, Noriyuki Kataoka², Taisuke Kageura⁵, Yoshihiko Takano⁶, Hiroshi Kawarada⁷, Tamio Oguchi⁸, Takayoshi Yokoya² & Tomohiro Matsushita¹

The electrical properties of diamond are modulated by impurity doping. Isolated substitutional boron atoms introduce holes; however, the fraction of electrically inactive boron atoms increases at higher doping concentrations. This has been attributed to boron aggregation and hydrogen passivation, although their structural identification based on atomic arrangement has yet to be experimentally verified. Here we show the origin of multiple chemical states in homoepitaxially grown boron-doped diamond thin films by analyzing the atomic environment of boron using spectro-photoelectron holography. Our analysis identifies boron dimers and boron-hydrogen complexes, with hydrogen occupying different atomic sites that give rise to distinct chemical shifts. These results suggest that hydrogen incorporation during growth leads to passivation of boron acceptors. We demonstrate that photoelectron holography serves as a promising tool for imaging hydrogen as well as determining the atomic sites of dopants.

Impurity doping is a fundamental technique for tuning the properties of functional materials. Trace levels of dopants can significantly influence the electrical and mechanical behavior of semiconductors and alloys¹. Accordingly, accurate knowledge of dopant positions and their surrounding atomic arrangement is essential for enhancing the predictive reliability of theoretical models and accelerating materials design. Nonetheless, direct observation of atomic arrangements without translational symmetry, such as isolated dopants, remains technically challenging.

In contrast, unintentional hydrogen incorporation in solids often leads to deleterious effects. In boron-doped diamonds (BDDs), a *p*-type semiconductor, hydrogen leads to carrier neutralization via dopant trapping¹. Additionally, hydrogen incorporation induces embrittlement in β -titanium alloys². Consequently, clarifying the

local behavior of hydrogen is necessary to understand its impact on material properties.

Various experimental techniques have been developed to characterize impurity distributions, including dopants and hydrogen. Scanning transmission electron microscopy (STEM) is a widely employed approach for analyzing the atomic arrangement of dopants. STEM image contrast is governed by the electron-scattering cross-sections of the constituent elements, enabling the detection of dopants within a matrix. However, elements with low scattering cross-sections are difficult to detect. Hydrogen, as the lightest element, presents particular challenges, with successful imaging largely confined to specialized systems, such as periodic hydrogen columns in the crystalline solid YH_2 ³. Atom probe tomography (APT) offers a promising approach for the direct observation of three-dimensional

¹Graduate School of Science and Technology, Nara Institute of Science and Technology, Nara, Japan. ²Research Institute for Interdisciplinary Science, Okayama University, Okayama, Japan. ³Department of Advanced Materials Science, Graduate School of Frontier Sciences, The University of Tokyo, Chiba, Japan. ⁴Material Innovation Research Center (MIRC), The University of Tokyo, Chiba, Japan. ⁵Sensing Technology Research Institute, National Institute of Advanced Industrial Science and Technology, Saga, Japan. ⁶Research Center for Materials Nanoarchitectonics, National Institute for Materials Science, Ibaraki, Japan. ⁷Faculty of Science and Engineering, Waseda University, Tokyo, Japan. ⁸Center for Spintronics Research Network, The University of Osaka, Osaka, Japan. ✉e-mail: tomita.hiroto.tf7@naist.ac.jp

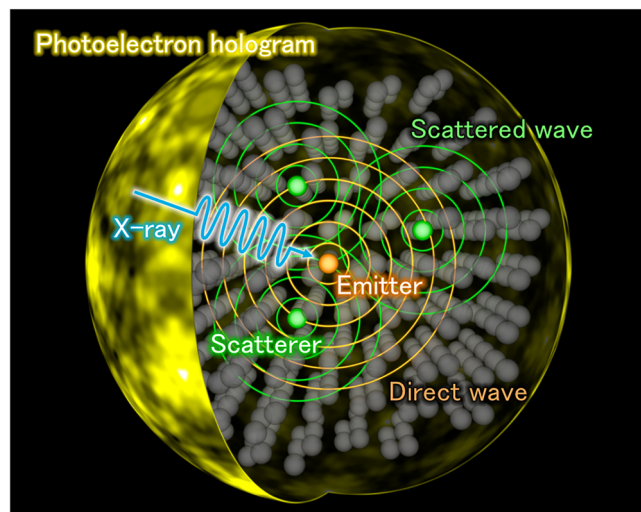


Fig. 1 | Principle of photoelectron hologram formation. Photoelectrons excited by incident light propagate as spherical waves. The interference between directly detected photoelectrons and those scattered by neighboring atoms generates the photoelectron hologram.

elemental distributions with sub-nanometer resolution. Recent APT studies have reported the direct detection of deuterium via deuterium-charging methods and cryogenic transfer protocols^{4–6}. While these reports provide valuable insights into hydrogen embrittlement mechanisms, distinguishing intrinsic hydrogen in solid solution from residual chamber gases requires rigorous assessment⁷. Although hydrogen behavior has been investigated using electron paramagnetic resonance⁸, elastic recoil detection analysis^{9,10}, secondary ion mass spectrometry¹¹, and neutron scattering^{12,13}, these methods lack the capability to directly observe local atomic arrangements around impurities. Therefore, a technique capable of visualizing hydrogen-containing impurities within the host matrix remains a critical need.

Photoelectron holography (PEH) has recently been applied as a technique for characterizing dopants, enabled by the development of high-throughput detectors and synchrotron radiation with high brightness and low emittance^{14–21}. These improvements enable the detection of dopants at concentrations near 0.1 at%^{14,16,18}. Figure 1 illustrates the principle of photoelectron hologram formation. Core-level photoelectrons emitted from dopants (emitters) propagate as spherical waves, referred to as direct waves. A fraction of these waves is scattered by the electrostatic potential of neighboring atoms (scatterers), generating additional spherical waves centered on the scatterers, referred to as scattered waves. The angular distribution of photoelectron intensity corresponds to the interference pattern of these waves. This is called a photoelectron hologram, which reflects the local three-dimensional atomic arrangement surrounding the emitter. In particular, the method of element- and chemical-state-selective analysis by measuring the kinetic-energy dependence of photoelectron holograms is called spectro-PEH. Since the scattering potential is primarily governed by the positive nuclear charge, light elements such as hydrogen are also detectable. X-ray photoelectron diffraction (XPD), a technique for measuring the same phenomenon as PEH, has also been increasingly reported in recent years^{22–26}. XPD patterns also exhibit emitter-site specificity^{27–29}. Given these similarities, this work adopts the terms “holography” and “hologram” throughout. Recent developments in photoelectron holography and diffraction are comprehensively reviewed elsewhere^{30–32}.

In this study, we applied spectro-PEH to investigate dopants in the BDD. In such materials, passivation of boron by hydrogen incorporation into the crystal lattice has been predicted³³. Consequently, the local behavior of hydrogen near boron sites has attracted significant

attention^{34–38}. We observed hydrogen atoms trapped by dopants. These findings clarify the origin of multiple chemical states observed in photoemission spectra and enable detailed characterization of BDD.

Results and Discussion

Evaluation of the crystallinity of the matrix by photoelectron holography

C 1s core-level photoelectron hologram measurements were performed to characterize the diamond lattice. The diamond unit cell contains two crystallographically inequivalent sites: the A site at (0, 0, 0) and the B site at (0.25, 0.25, 0.25). The crystal structures as viewed from each site are presented in Fig. 2a, b. The experimentally obtained hologram represents the sum of contributions from both sites. The left image in Fig. 2c shows the experimentally obtained C 1s hologram recorded at a kinetic energy (E_k) of ~610 eV, which closely matches prior diamond C 1s holograms reported by Küttel et al.³⁹ and Yokoya et al.¹⁶. The right image of Fig. 2c presents a simulated hologram based on a pristine diamond cluster. Fig. 2d illustrates atomic positions as viewed from the emitter along the <111> direction. Both experimental and simulated patterns display prominent forward focusing peaks (FFPs) originating from atoms aligned along the <001>, <111>, and <110> directions. The dark features marked by dashed white lines are identified as quasi-Kikuchi lines, which arise from Bragg-like scattering and interference ring overlap, indicating long-range crystallographic order^{31,40}. The simulation accurately reproduces both the FFPs and the crescent-shaped fine structure near the <001> direction, confirming the high crystallinity of the BDD thin film.

Spectro-photoelectron holography for B 1s core-level

B 1s core-level photoemission spectra were measured and fitted utilizing the parameters established by Okazaki et al.⁴¹, as displayed in Fig. 3a. The lowest binding energy component (component 1) exhibits the narrowest peak width, consistent with prior observations⁴¹. Components 5, 6, and 7 are attributed to boron atoms near the surface, a conclusion supported by the spectra's emission-angle dependence. This paper focuses on components 1–4. The photoelectron hologram of component 1 in Fig. 3b closely resembles the experimental C 1s hologram, indicating boron substitution at a carbon site, in agreement with Okazaki et al.⁴¹. Consequently, component 1 is assigned to isolated substitutional boron (B_S). The simulated hologram in Fig. 3c, based on the B_S model in Fig. 3d, accurately reproduces the primary features of the component 1 pattern. These results demonstrate that spectro-PEH effectively identifies boron atoms substituted at electrically active sites.

Structural determination of boron dimer

Figure 4a shows the experimental hologram of component 4 in the B 1s core-level. Although prominent FFPs are preserved, the hologram displays pattern broadening relative to the component 1 hologram; fine structures in the <111> and <110> directions are less defined. The line profile at the left of Fig. 4a shows the disappearance of the sharp peaks and valleys characteristic of component 1, resulting in reduced contrast. Such broadening suggests that boron atoms are displaced from ideal substitutional lattice sites. The photoelectron hologram is sensitive to emitter position shifts. A pioneering study by Fedchenko et al. demonstrated the disappearance of Kikuchi lines caused by sub-angstrom-scale relaxation of the emitter²⁷. Prior theoretical investigations^{42–48} propose two structural candidates to account for atomic shifts: a hydrogen atom located at the center of a B–C bond, forming a B–H complex with bond-center configuration (Fig. 4b), and a nearest-neighbor boron pair (B dimer), as shown in Fig. 4c⁴⁶. Figure 4d shows the simulated hologram of the B–H complex with bond-center configuration. The simulation indicates that insertion of hydrogen within the B–C bond produces a large emitter displacement (B–H–

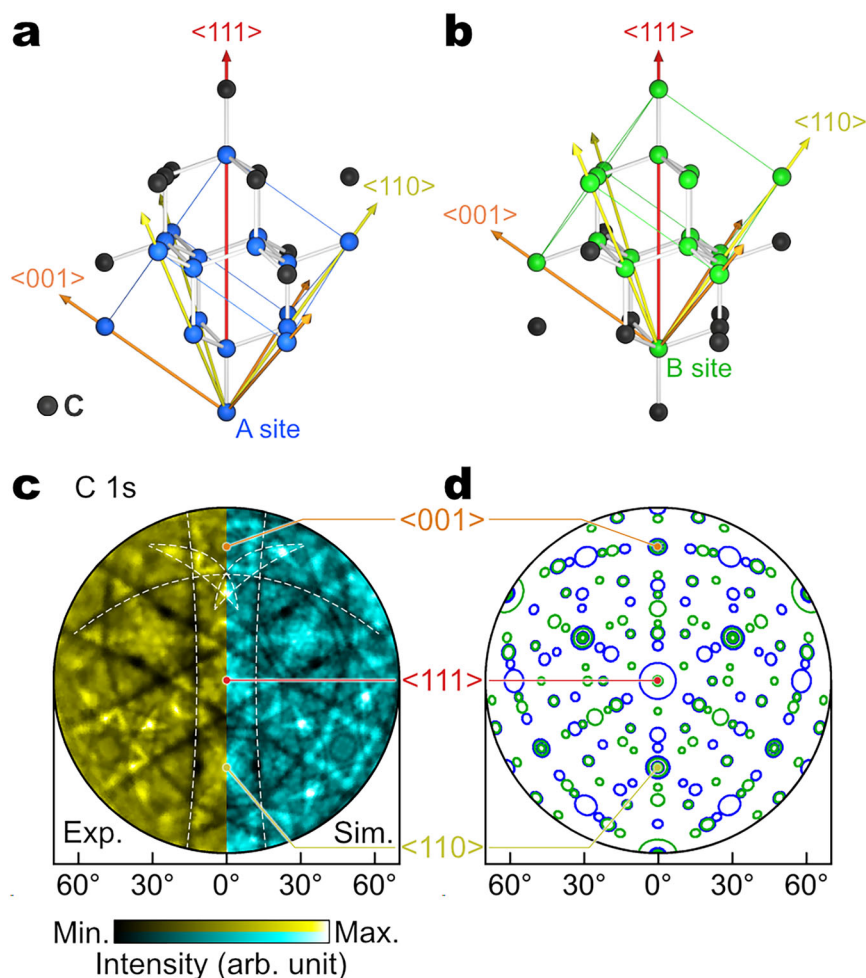


Fig. 2 | Photoelectron hologram of the diamond matrix. Diamond crystal structures with carbon atoms at (a) the A site and (b) the B site as emitters. Blue and green spheres represent the local atomic environment for emitters at the A and B sites, respectively. **c** Comparison of an experimental C 1s core-level photoelectron hologram obtained from the boron-doped diamond (111) thin film (left) and a

simulated hologram based on pristine diamond (right). The centers of the holograms correspond to the $\langle 111 \rangle$ direction. **d** Projected atomic positions within an 8 Å radius of the emitters. Blue and green circles correspond to views from the A and B sites, respectively; the circle size scales with proximity to the emitter. Source data are provided as a source data file.

C $\approx 2.21 \text{ Å}^{46}$, 2.22 Å^{45}), yielding a pattern that diverges drastically from the experimental pattern of component 4; thus, the bond-center configuration is excluded from the candidate model. In contrast, relaxation calculations predict a modest displacement for the B dimer ($\approx 0.20 \text{ Å}^{46}$), and the simulated hologram of B dimer (Fig. 4e) preserves the substitutional-site pattern while capturing the observed broadening. Accordingly, component 4 is attributed to boron atoms arranged in the B dimer configuration. The atomic arrangement yielding the highest similarity to the experimental image was determined by minimizing the root mean squared error (RMSE). A grid search method optimized the boron position parameters. As shown in Fig. 4f, the extracted B–B distance is 2.04 Å , indicating an elongation relative to a C–C bond length of 1.57 Å and in agreement with theoretical values of 1.94 Å^{49} , 1.97 Å^{46} and 1.99 Å^{49} .

Detection of hydrogen trapped by boron

Figure 5a, b demonstrate that the photoelectron holograms of components 2 and 3 closely resemble that of component 1. To visualize structural deviations from the B_s configuration, these patterns were divided by the component 1 pattern. The resulting ratio images are displayed in the left panels of Fig. 5e, f. The component 2/1 ratio image exhibits bright regions along the $\langle 001 \rangle$ direction (orange dashed line), whereas the component 3/1 ratio image exhibits bright regions along the $\langle 111 \rangle$ direction (red dashed lines). Horie

et al. previously demonstrated that oxygen vacancies manifest as dark regions in ratio images²¹. Conversely, the bright regions observed in this study indicate the presence of additional hydrogen atoms surrounding the substitutional boron.

In the component 2/1 ratio image, the bright regions along the $\langle 001 \rangle$ direction suggest that hydrogen atoms occupy bridging sites, as shown in Fig. 5c. A simulated hologram of an atomic cluster without carbon atoms, based on the B–H complex with bridging site configuration proposed by a first-principles calculation⁴⁶, is presented in the right panel of Fig. 5e. This model utilizes a B–H distance of 1.20 Å^{46} . The bright regions in the experimental ratio image exhibit excellent agreement with the simulation.

On the other hand, the bright regions along the $\langle 111 \rangle$ direction in the component 3/1 ratio image suggest the presence of hydrogen at the anti-bonding site, as shown in Fig. 5d. The right panel of Fig. 5f displays a simulated hologram based on the B–H complex with anti-bonding configuration, incorporating a B–H distance of 1.17 Å^{46} . The FFPs in the simulation accurately reproduce the experimental features along the $\langle 111 \rangle$ direction.

In the B 1s core-level photoemission spectrum, components 2 and 3 exhibit a chemical shift toward higher binding energy compared to component 1 of the B_s configuration, indicating that the boron in the B–H complex possesses a greater positive charge, while the neighboring hydrogen behaves in a proton-like state. The peak areas of components

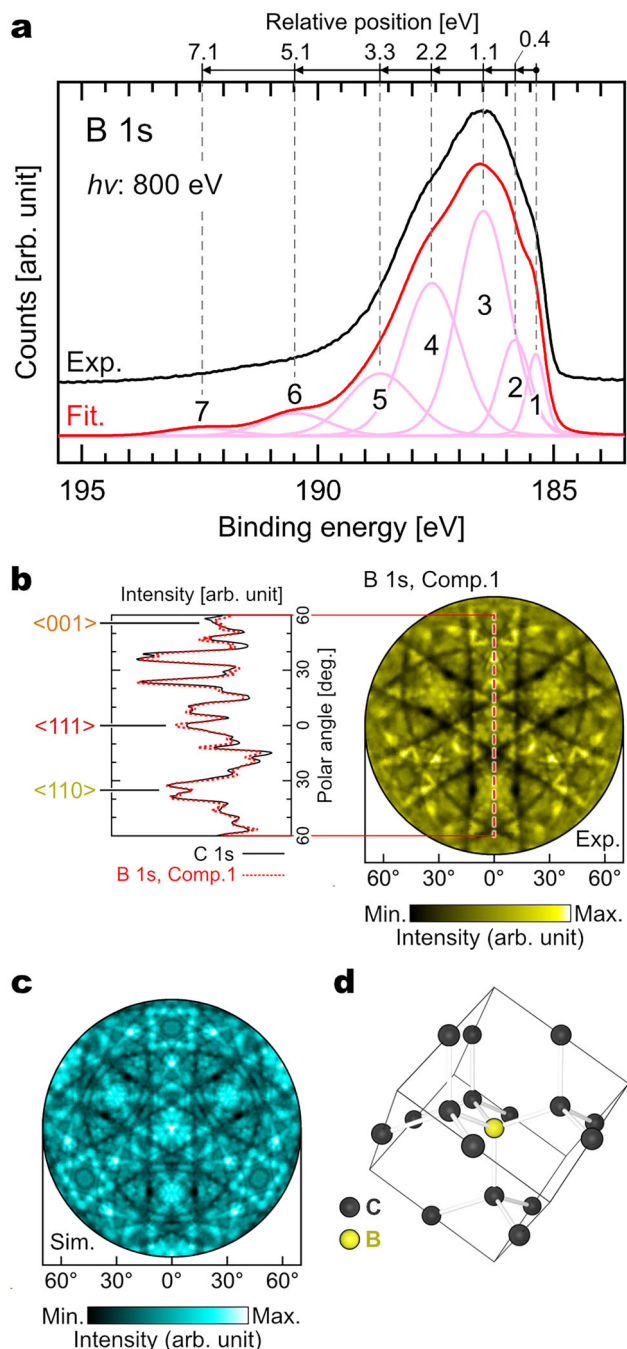


Fig. 3 | Spectro-photoelectron holography analysis of the B 1s core-level. **a** B 1s core-level photoemission spectrum obtained from the boron-doped diamond thin film. Following Shirley-type background subtraction, the spectrum was fitted using symmetric Voigt functions. Relative energy positions with respect to component 1 are indicated at the top. For details, refer to the source data. **b** An experimental hologram of component 1 in the B 1s core-level. The left graph displays intensity line profiles comparing the emission-angle dependence of the C 1s (solid black line) and component 1 in B 1s (dashed red line). **c** A simulated hologram based on the isolated substitutional boron model shown in **d**. Source data are provided as a source data file.

2 and 3 indicate that boron at the B–H complex with anti-bonding site configuration is approximately 3.8 times more abundant than in the bridging site configuration. Most theoretical studies conclude that the bridge site model is more stable^{45–47,50–52}. However, the small difference in formation energies between the two configurations, coupled with the fact that the experimental abundance ratios were obtained under

limited temperature conditions, suggests that the results are not significantly inconsistent with theoretical predictions.

Spectro-PEH revealed the atomic arrangement surrounding the dopants in the boron-doped diamond thin film. The chemical shift observed in the B 1s core-level photoemission spectra is attributed to the formation of boron aggregates and B–H complexes, as confirmed by photoelectron holograms. Ratio images identify the trapping sites of hydrogen atoms neighboring boron. These defect structures arise from hydrogen introduced during crystal growth and from hydrogen etching. In conclusion, spectro-PEH effectively correlates core-level spectral shifts with atomic arrangement and presents a promising tool for imaging hydrogen atoms.

Methods

Sample preparation

A boron-doped diamond thin film was homoepitaxially grown on a high-pressure and high-temperature (HPHT) synthetic type Ib (111)-oriented single-crystal diamond substrate using an ASTeX microwave plasma-assisted chemical vapor deposition (MPCVD) apparatus^{53–58}. Trimethylboron [B(CH₃)₃], diluted in hydrogen and methane, served as the dopant source. The gas phase composition was controlled with a methane concentration of 5% and a trimethylboron/methane ratio ([B(CH₃)₃]/[CH₄]) of 9000 ppm, while the total gas flow rate was maintained at 100 sccm. Based on the growth rate, the film thickness was calculated to be approximately 300 nm. Synthesis pressure and substrate temperature were maintained at 110 Torr and 800 °C, respectively. Following synthesis, the sample was boiled in a 1:3 mixture of HNO₃ and H₂SO₄ at 200 °C for 30 minutes to ensure surface oxygen termination. The boron concentration, estimated by SIMS, was $8\text{--}10 \times 10^{21} \text{ cm}^{-3}$ (4.5 at%). The superconducting transition temperature determined via the four-point probe method was 10.0 K. The sample was annealed at 500 °C under ultrahigh vacuum to reduce oxygen-related contaminations on the surface.

Spectro-photoelectron holography experiments

Spectro-photoelectron holography experiments were conducted at the soft X-ray beamline BL25SU in SPring-8, Japan, utilizing a Scienta Omicron DA30 electron energy analyzer. Measurements were acquired at room temperature with unpolarized synchrotron radiation. The Fermi-edge of the molybdenum sample holder served as the calibration standard for binding energy. The total energy resolution was set to be ~200 meV. The angle between the beam axis and the sample surface was set at 5°. Supplementary Fig. 1 illustrates experimental geometry. The DA30 analyzer simultaneously captures photoelectron angular dispersion and kinetic energy (E_k) along the longitudinal slit direction (θ_x) within an acceptance angle of $\pm 15^\circ$. Furthermore, a built-in deflector permits analysis of the angular dispersion in the transverse direction (θ_y) up to a deflection angle of $\pm 10^\circ$. Muro et al. provide a comprehensive description of the experimental apparatus⁵⁹.

The kinetic energy dependence of the photoemission intensity angular distribution (θ_x , θ_y , E_k) was acquired by scanning the sample's polar angle ($\theta = 0\text{--}70^\circ$) and in-plane rotation angle ($\varphi = 0\text{--}120^\circ$). In this three-dimensional dataset, the E_k axis represents the photoelectron spectrum. The acquisition of 158,400 photoemission spectra for a single hologram required approximately 66 hours.

Data processing for spectro-photoelectron holography

The following data processing was performed based on the methodology described in Matsushita et al.⁶⁰. Peak fitting was applied to the measured spectra to retrieve two-dimensional intensity distributions. Following Shirley-type background subtraction, the spectra were fitted using symmetric Voigt functions (a convolution of Gaussian and Lorentzian). Refer to the source data for detailed fitting parameters. The resulting images correspond to the two-dimensional

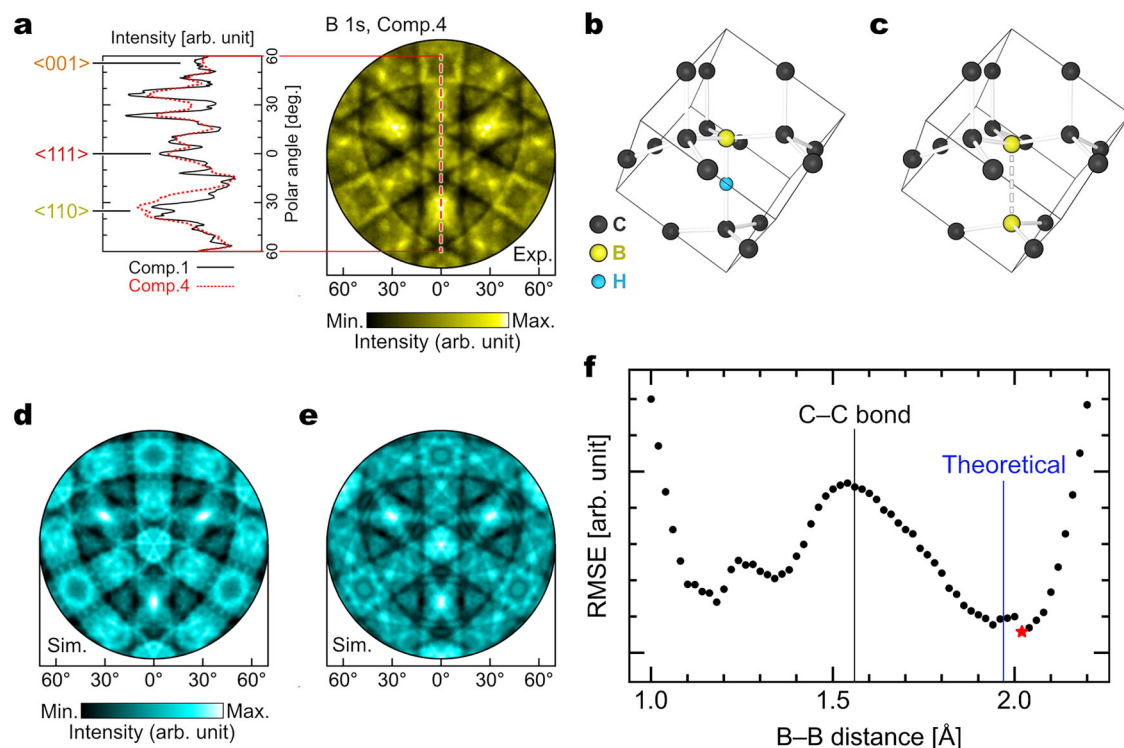


Fig. 4 | Pattern broadening induced by atomic position shifts in the B dimer. **a** An experimentally obtained photoelectron hologram of component 4 in the B 1s core-level. The left graph displays intensity line profiles comparing the emission angle dependence of component 1 (solid black line) and component 4 (dashed red line). **b**, **c** illustrate schematics of the B-H complex with bond-center configuration and the B

dimer, respectively. **d**, **e** are simulated holograms using the models in (**b**) and (**c**), respectively. **f** Root mean square error (RMSE) values between the component 4 hologram and simulated holograms based on the B dimer, with variations in boron atomic positions. Black dots indicate sampling points; the red star denotes the configuration with the highest similarity. Source data are provided as a source data file.

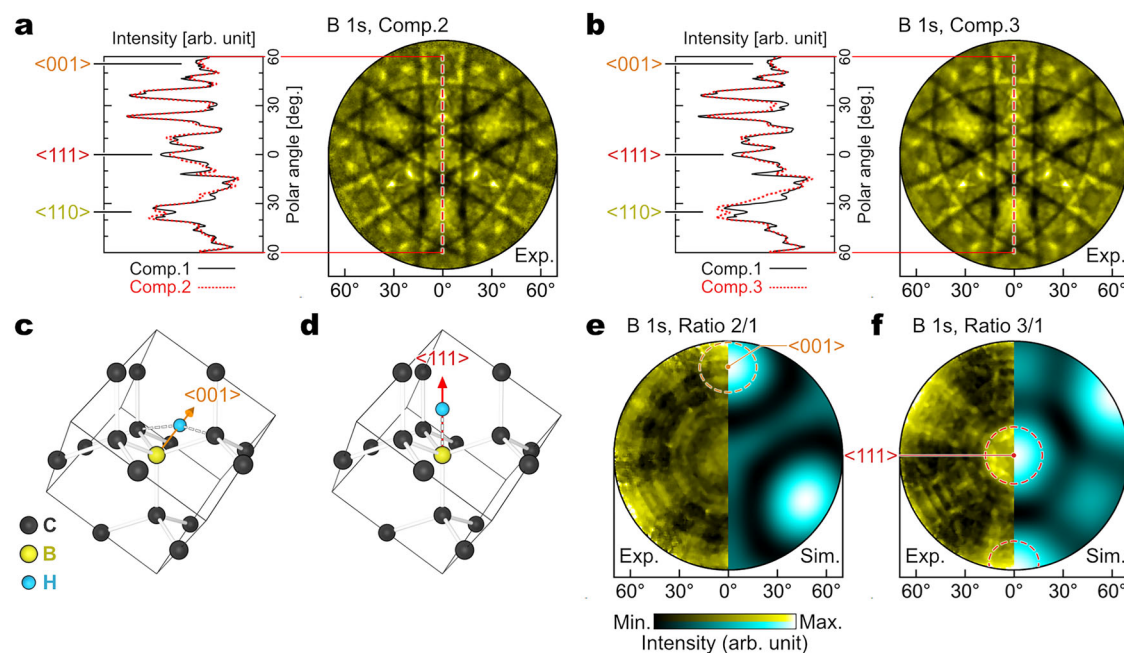


Fig. 5 | Photoelectron holograms of the B-H complexes. **a** An experimentally obtained photoelectron hologram of component 2 in the B 1s core-level. The left graph displays intensity line profiles comparing the emission-angle dependence of component 1 (solid black line) and component 2 (dashed red line). **b** An experimentally obtained photoelectron hologram of component 3 in the B 1s core-level. The left graph displays intensity line profiles comparing the emission-angle dependence of component 1 (solid black line) and component 3 (dashed red line). Schematics of the B-H complex with (**c**) bridging site and (**d**) anti-bonding site

configuration. **e** A component 2/1 ratio image (left) and a simulated hologram based on a B-H complex model with bridging site configuration without carbon atoms, where hydrogen is aligned in the <001> direction (right). The orange dashed circle highlights the bright region in the <001> direction. **f** A component 3/1 ratio image (left) and a simulated hologram based on a B-H complex model with anti-bonding configuration without carbon atoms, where hydrogen is aligned in the <111> direction (right). The red dashed circle highlights the bright region in the <111> direction. Source data are provided as a source data file.

photoemission intensity angular distribution within the range of $\pm 15^\circ \times \pm 10^\circ$ (hologram fragment).

The hologram fragments were mapped to equidistant cylindrical projection with a 0.5° grid. Angular calibration of the C 1s hologram fragments was performed referencing simulated patterns based on pristine diamond. Obtained calibration parameter utilized for the B 1s hologram fragments. Then we composed a hologram from all fragments. The final hologram was obtained by symmetrizing the composited image to take into account the symmetry of diamond structure. All photoelectron holograms shown in this paper are projected using an azimuthal equidistant projection.

Photoelectron hologram simulations

Hologram calculations were performed using the total analysis multiple scattering pattern simulation code (TMSP), which utilizes the partial-wave expansion method for spherical waves⁶¹. The calculations incorporate the electron inelastic mean free path (IMFP) and the Debye-Waller factor⁴⁰. Although calculating scattering from individual atoms within a finite cluster is computationally intensive, this approach enables the analysis of aperiodic systems without relying on periodic boundary conditions. For photoelectron kinetic energies between 100 eV and several keV, backscattering makes a negligible contribution and is excluded from the simulations.

Simulation parameters were optimized using the experimentally obtained C 1s hologram. A grid search identified the cluster size and IMFP that minimized the RMSE, as shown in Supplementary Fig. 2. The optimal IMFP was determined to be 14 Å, consistent with the theoretical value of 13.95 Å derived from the JPT formula for an electron with a kinetic energy of 610 eV in diamond⁶². This parameter accounts for signal attenuation due to distant scatterers⁴⁰. Regarding cluster size, the RMSE plateaued near a radius of 17 Å. Therefore, to balance computational efficiency with reconstruction accuracy, a cluster radius of 20 Å and an IMFP of 14 Å were adopted for all simulations.

Reporting summary

Further information on research design is available in the Nature Portfolio Reporting Summary linked to this article.

Data availability

The source data for Figs. 2–5 are provided as a source data file. All raw data that supports the findings of this study are available from the corresponding author upon request. Source data are provided with this paper.

References

- Hayashi, K. et al. Investigation of the effect of hydrogen on electrical and optical properties in chemical vapor deposited on homo-epitaxial diamond films. *J. Appl. Phys.* **81**, 744–753 (1997).
- Froes, F. H., Senkov, O. N. & Qazi, J. I. Hydrogen as a temporary alloying element in titanium alloys: Thermohydrogen processing. *Int. Mater. Rev.* **49**, 227–245 (2004).
- Ishikawa, R. et al. Direct imaging of hydrogen-atom columns in a crystal by annular bright-field electron microscopy. *Nat. Mater.* **10**, 278–281 (2011).
- Takahashi, J., Kawakami, K. & Tarui, T. Direct observation of hydrogen-trapping sites in vanadium carbide precipitation steel by atom probe tomography. *Scr. Mater.* **67**, 213–216 (2012).
- Chen, Y.-S. et al. Direct observation of individual hydrogen atoms at trapping sites in a ferritic steel. *Science* **355**, 1196–1199 (2017).
- Chen, Y.-S., Bagot, P. A. J., Moody, M. P. & Haley, D. Observing hydrogen in steel using cryogenic atom probe tomography: A simplified approach. *Int. J. Hydrog. Energy* **44**, 32280–32291 (2019).
- Chang, Y. et al. Characterizing solute hydrogen and hydrides in pure and alloyed titanium at the atomic scale. *Acta Mater.* **150**, 273–280 (2018).
- Fernadi Lukman, M. & Pöppel, A. Electron paramagnetic resonance spectroscopy: Toward the path of dihydrogen isotopologue detection in porous materials. <https://doi.org/10.1039/D4CC06430E> (2025).
- Torrìsi, L. & Cutroneo, M. Elastic recoil detection analysis (ERDA) in hydrogenated samples for TNSA laser irradiation. *Surf. Interface Anal.* **48**, 10–16 (2016).
- Topić, M., Halindintwali, S., Mtshali, C., Nsengiyumva, S. & Khumalo, Z. M. Hydrogen storage in Ti-based metal hydrides investigated by elastic recoil detection analysis (ERDA). *Nucl. Instrum. Methods Phys. Res. Sect. B Beam Interact. Mater.* **450**, 239–243 (2019).
- Tarzimoghadam, Z. et al. Multi-scale and spatially resolved hydrogen mapping in a Ni-Nb model alloy reveals the role of the δ phase in hydrogen embrittlement of alloy 718. *Acta Mater.* **109**, 69–81 (2016).
- Amann-Winkel, K. et al. X-ray and neutron scattering of water. *Chem. Rev.* **116**, 7570–7589 (2016).
- Parker, B. S. F. & Collier, P. Applications of neutron scattering in catalysis: Where atoms are and how they move. *Johns. Matthey Technol. Rev.* **60**, 132–144 (2016).
- Tsutsui, K. et al. Individual atomic imaging of multiple dopant sites in As-doped Si using spectro-photoelectron holography. *Nano Lett.* **17**, 7533–7538 (2017).
- Matsui, F., Matsushita, T. & Daimon, H. Holographic reconstruction of photoelectron diffraction and its circular dichroism for local structure probing. *J. Phys. Soc. Jpn.* **87**, 061004 (2018).
- Yokoya, T. et al. Asymmetric phosphorus incorporation in homo-epitaxial P-doped (111) diamond revealed by photoelectron holography. *Nano Lett.* **19**, 5915–5919 (2019).
- Uenuma, M. et al. Atomic structure analysis of gallium oxide at the Al₂O₃/GaN interface using photoelectron holography. *Appl. Phys. Express* **15**, 085501 (2022).
- Tang, J. et al. Direct observation of atomic structures and chemical states of active and inactive dopant sites in Mg-doped GaN. *ACS Appl. Electron. Mater.* **4**, 4719–4723 (2022).
- Takeuchi, S., Hashimoto, Y., Daimon, H. & Matsushita, T. High-precision atomic image reconstruction from photoelectron hologram of O on W(110) by SPEA-L1. *J. Electron Spectrosc. Relat. Phenom.* **256**, 147177 (2022).
- Fujii, M. N. et al. Atomic imaging of interface defects in an insulating film on diamond. *Nano Lett.* **23**, 1189–1194 (2023).
- Horie, R. et al. Origin of unexpected Ir³⁺ in a superconducting candidate Sr₂IrO₄ system analyzed by photoelectron holography. *Inorg. Chem.* **62**, 10897–10904 (2023).
- Saldin, D. K., Harp, G. R. & Chen, X. Concentric-shell algorithm for auger and core-level photoelectron diffraction: Theory and applications. *Phys. Rev. B* **48**, 8234–8244 (1993).
- Chen, Y. et al. Convergence and reliability of the rehr-albers formalism in multiple-scattering calculations of photoelectron diffraction. *Phys. Rev. B* **58**, 13121–13131 (1998).
- García De Abajo, F. J., Van Hove, M. A. & Fadley, C. S. Multiple scattering of electrons in solids and molecules: A cluster-model approach. *Phys. Rev. B* **63**, 075404 (2001).
- Viana, M. L., Díez, Muiño, R., Soares, E. A., Van Hove, M. A. & De Carvalho, V. E. Global search in photoelectron diffraction structure determination using genetic algorithms. *J. Phys. Condens. Matter* **19**, 446002 (2007).
- Winkelmann, A., Fadley, C. S. & Garcia De Abajo, F. J. High-energy photoelectron diffraction: model calculations and future possibilities. *New J. Phys.* **10**, 113002 (2008).
- Fedchenko, O. et al. Emitter-site specificity of hard x-ray photoelectron Kikuchi-diffraction. *New J. Phys.* **22**, 103002 (2020).
- Medjanik, K. et al. Site-specific atomic order and band structure tailoring in the diluted magnetic semiconductor (In,Ga,Mn)As. *Phys. Rev. B* **103**, 075107 (2021).
- Hoesch, M. et al. Active sites of Te-hyperdoped silicon by hard x-ray photoelectron spectroscopy. *Appl. Phys. Lett.* **122**, 252108 (2023).

30. Kuznetsov, M. V. et al. Photoelectron diffraction and holography studies of 2D materials and interfaces. *J. Phys. Soc. Jpn.* **87**, 061005 (2018).
31. Fedchenko, O., Winkelmann, A. & Schönhense, G. Structure analysis using time-of-flight momentum microscopy with hard X-rays: Status and prospects. *J. Phys. Soc. Jpn.* **91**, 091006 (2022).
32. Yokoya, T. Photoelectron diffraction and holography studies on dopant local structures. *J. Phys. Soc. Jpn.* **91**, 091007 (2022).
33. Chevallier, J. et al. Hydrogen-boron interactions in p-type diamond. *Phys. Rev. B* **58**, 7966–7969 (1998).
34. Chevallier, J. et al. Hydrogen in monocrystalline CVD boron-doped diamond. *Phys. Status Solidi A* **174**, 73–81 (1999).
35. Teukam, Z. et al. Shallow donors with high n-type electrical conductivity in homoepitaxial deuterated boron-doped diamond layers. *Nat. Mater.* **2**, 482–486 (2003).
36. Mukuda, H. et al. 11B-NMR study in boron-doped diamond films. *Sci. Technol. Adv. Mater.* **7**, S37 (2006).
37. Murakami, M., Shimizu, T., Tansho, M. & Takano, Y. 11B nuclear magnetic resonance in boron-doped diamond. *Sci. Technol. Adv. Mater.* **9**, 044103 (2009).
38. Barjon, J. et al. Hydrogen-induced passivation of boron acceptors in monocrystalline and polycrystalline diamond. *Phys. Chem. Chem. Phys.* **13**, 11511 (2011).
39. Küttel, O. M., Agostino, R. G., Fasel, R., Osterwalder, J. & Schlapbach, L. X-ray photoelectron and Auger electron diffraction study of diamond and graphite surfaces. *Surf. Sci.* **312**, 131–142 (1994).
40. Matsushita, T. et al. Theory for high-angular-resolution photoelectron holograms considering the inelastic mean free path and the formation mechanism of quasi-kikuchi band. *Phys. Status Solidi B* **257**, 2000117 (2020).
41. Okazaki, H. et al. Soft X-ray core-level photoemission study of boron sites in heavily boron-doped diamond films. *J. Phys. Soc. Jpn.* **78**, 034703 (2009).
42. Goss, J. P. et al. Deep hydrogen traps in heavily B-doped diamond. *Phys. Rev. B* **68**, 235209 (2003).
43. Goss, J. P. & Briddon, P. R. Theory of boron aggregates in diamond: First-principles calculations. *Phys. Rev. B* **73**, 085204 (2006).
44. Goss, J. P., Eyre, R. J. & Briddon, P. R. Theoretical models for doping diamond for semiconductor applications. *Phys. Status Solidi B* **245**, 1679–1700 (2008).
45. Kumar, A., Pernot, J., Deneuville, A. & Magaud, L. Ab initio study of boron-hydrogen complexes in diamond and their effect on electronic properties. *Phys. Rev. B* **78**, 235114 (2008).
46. Oguchi, T. Electronic structure of boron-doped diamond with B–H complex and B pair. *Sci. Technol. Adv. Mater.* **9**, 044211 (2008).
47. Upadhyay, A., Singh, A. K. & Kumar, A. Electronic structure and stability of hydrogen defects in diamond and boron doped diamond: A density functional theory study. *Comput. Mater. Sci.* **89**, 257–263 (2014).
48. Watanabe, T. et al. The local structure in heavily boron-doped diamond and the effect this has on its electrochemical properties. *Carbon* **137**, 333–342 (2018).
49. Long, R. et al. Effect of B-complexes on lattice structure and electronic properties in heavily boron-doped diamond. *Diam. Relat. Mater.* **17**, 234–239 (2008).
50. Dai, Y., Dai, D., Liu, D., Han, S. & Huang, B. Mechanism of p-type-to-n-type conductivity conversion in boron-doped diamond. *Appl. Phys. Lett.* **84**, 1895–1897 (2004).
51. Goss, J. P., Briddon, P. R., Sque, S. J. & Jones, R. Boron-hydrogen complexes in diamond. *Phys. Rev. B* **69**, 165215 (2004).
52. Lombardi, E. B., Mainwood, A. & Osuch, K. Interaction of hydrogen with boron, phosphorus, and sulfur in diamond. *Phys. Rev. B* **70**, 205201 (2004).
53. Takano, Y. et al. Superconductivity in diamond thin films well above liquid helium temperature. *Appl. Phys. Lett.* **85**, 2851–2853 (2004).
54. Takano, Y. et al. Superconductivity in polycrystalline diamond thin films. *Diam. Relat. Mater.* **14**, 1936–1938 (2005).
55. Yokoya, T. et al. Origin of the metallic properties of heavily boron-doped superconducting diamond. *Nature* **438**, 647–650 (2005).
56. Takano, Y. et al. Superconducting properties of homoepitaxial CVD diamond. *Diam. Relat. Mater.* **16**, 911–914 (2007).
57. Kawano, A. et al. Superconductor-to-insulator transition in boron-doped diamond films grown using chemical vapor deposition. *Phys. Rev. B* **82**, 085318 (2010).
58. Okazaki, H. et al. Signature of high T_c above 25 K in high quality superconducting diamond. *Appl. Phys. Lett.* **106**, 052601 (2015).
59. Muro, T. et al. Soft X-ray ARPES for three-dimensional crystals in the micrometre region. *J. Synchrotron Radiat.* **28**, 1631–1638 (2021).
60. Matsushita, T., Muro, T., Matsui, F., Happo, N. & Hayashi, K. Data processing for atomic resolution holography. *Jpn. J. Appl. Phys.* **59**, 020502 (2020).
61. Matsushita, T., Matsui, F., Daimon, H. & Hayashi, K. Photoelectron holography with improved image reconstruction. *J. Electron Spectrosc. Relat. Phenom.* **178–179**, 195–220 (2010).
62. Jablonski, A., Tanuma, S. & Powell, C. J. Calculations of electron inelastic mean free paths (IMFPs). XIV. Calculated IMFPs for LiF and Si₃N₄ and development of an improved predictive IMFP formula. *Surf. Interface Anal.* **55**, 609–637 (2023).

Acknowledgements

The authors thank Dr. Muro for his support in developing the experimental apparatus and for his support during the experiments. The synchrotron radiation experiments were performed with the approval of JASRI proposal number 2018A1161 (T.Y.). This work was supported by JSPS Grants-in-Aid for Transformative Research Area (A) “Hyper-Ordered Structures Science” grant numbers 20H05882 (T.Y.) and 20H05884 (T.M.); JSPS KAKENHI grant numbers 20H01841 (T.M.) and 21K18184 (T.M.); JSPS Program for Forming Japan’s Peak Research Universities (J-PEAKS) grant number JPJS00420230010. This study was conducted with support from Nara Institute of Science and Technology, Data Science Center, RX Platform Organizational Development Project, funded by MEXT’s Education and Research Organization Reform Project (T.M.).

Author contributions

W.H., T.T., H.F., and N.K. performed measurements. T.K. and Y.T. prepared the sample. H.T. analyzed the experimental results. T.M. provided simulation and analysis software. T.O., H.K., and T.Y. supervised the project. All authors contributed to the writing of the manuscript.

Competing interests

The authors declare no competing interests.

Additional information

Supplementary information The online version contains supplementary material available at <https://doi.org/10.1038/s41467-026-70231-7>.

Correspondence and requests for materials should be addressed to Hiroto Tomita.

Peer review information *Nature Communications* thanks the anonymous reviewers for their contribution to the peer review of this work. A peer review file is available.

Reprints and permissions information is available at <http://www.nature.com/reprints>

Publisher’s note Springer Nature remains neutral with regard to jurisdictional claims in published maps and institutional affiliations.

Open Access This article is licensed under a Creative Commons Attribution-NonCommercial-NoDerivatives 4.0 International License, which permits any non-commercial use, sharing, distribution and reproduction in any medium or format, as long as you give appropriate credit to the original author(s) and the source, provide a link to the Creative Commons licence, and indicate if you modified the licensed material. You do not have permission under this licence to share adapted material derived from this article or parts of it. The images or other third party material in this article are included in the article's Creative Commons licence, unless indicated otherwise in a credit line to the material. If material is not included in the article's Creative Commons licence and your intended use is not permitted by statutory regulation or exceeds the permitted use, you will need to obtain permission directly from the copyright holder. To view a copy of this licence, visit <http://creativecommons.org/licenses/by-nc-nd/4.0/>.

© The Author(s) 2026